# Journal of Materials Chemistry A

Accepted Manuscript


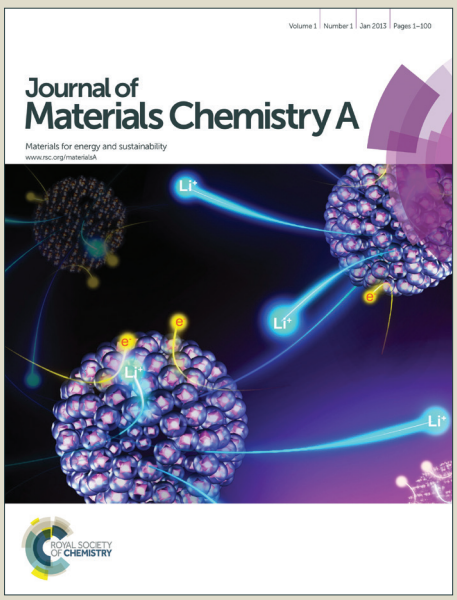





ROYAL SOCIETY OF CHEMISTRY

www.rsc.org/materialsA

**Electrospun lead-doped titanium dioxide nanofibers and in situ preparation perovskite-sensitized photoanodes for use in high performance perovskite solar cells**

Yaoming Xiao*, Gaoyi Han*, Yanping Li and Miaoyu Li

Perovskite-sensitized $TiO_2$ nanofibers (TNFs) are firstly prepared by an electrospun and in situ method. The electrospun TNFs can provide direct pathways for the rapid collection and transmission of photogenerated electrons. The photoanode based on the in situ method shows not only excellent contacting between the TNF and perovskite, but also abundant perovskite filling in it. These can be conducive not only to the separation and transmission of the electron and hole, but also to the absorption and utilization of sunlight.

Keywords: electrospun, in situ method, titanium dioxide nanofiber, photoanode, perovskite solar cell

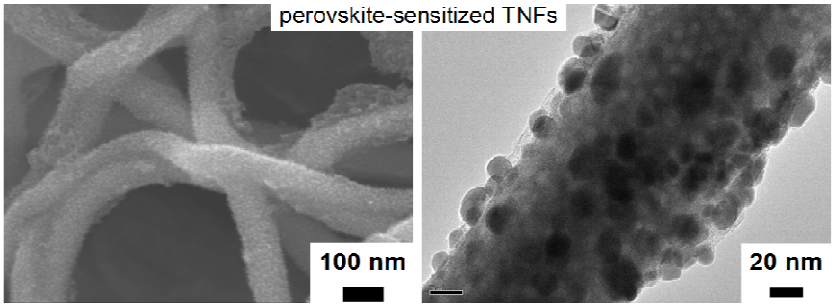


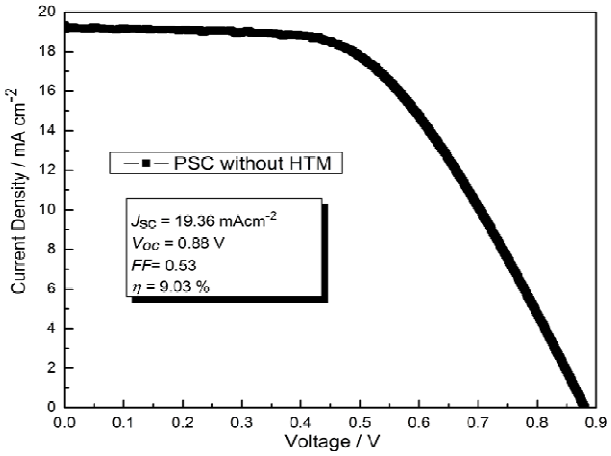

# Electrospun lead-doped titanium dioxide nanofibers and in situ preparation perovskite-sensitized photoanodes for use in high performance perovskite solar cells

**Yaoming Xiao*, Gaoyi Han*, Yanping Li and Miaoyu Li**

**Abstract:** Lead-doped $TiO_2$ nanofibers (TNFs) are fabricated by using an electrospun method, and then in situ preparation perovskite-sensitized photoanode for use in the perovskite solar cell (PSC). The electrospun TNFs can provide direct pathways for the rapid collection and transmission of photogenerated electrons. The photoanode based on the in situ method shows not only excellent contacting between the TNF and perovskite, but also abundant perovskite filling in it. These can be conducive not only to the separation and transmission of the electron and hole, but also to the absorption and utilization of sunlight. Finally a high performance PSC with 9.03% of the cell efficiency is obtained without any hole transporting materials.

**Keywords:** electrospun, in situ method, titanium dioxide nanofiber, photoanode, perovskite solar cell.

## Introduction

Organolead halide perovskites ($CH_3NH_3PbX_3$, X = I, Br, and Cl) have been attracted extensive attention as light harvesters for high performance perovskite solar cells (PSCs) over the last few years, due to their optimal band gap, wide light absorption, and long-range exciton diffusion lengths.[1-9] The PSC shows an impressive high open circuit voltage, high power conversion

efficiency, and long-term stability in conjunction with the development of new device architectures,[2,3,5,6] deposition methods,[1,4] and hole transporting materials (HTMs).[10-12]

In order to improve the photovoltaic performance of the $TiO_2$ photoanode, many efforts have been devoted to the design and synthesis of $TiO_2$ with particular structures, such as nanotube,[13,14] nanorod,[15] and nanowire.[16-18] The particular structures have been proved successfully for the dye-sensitized solar cell and the PSC, since they can provide direct pathways for the rapid collection of photogenerated electrons, which could improve the photovoltaic performance of the device.[19,20] There are two major deposition methods for the preparation of PSCs. On the one hand, one-step[2,3,5,21-24] or two-step[1] solution process was used to fabricate the perovskite sensitized $TiO_2$ photoanode. As a result, two-step method could obtain higher performance PSC than that of the one-step method due to its more controllable size of the perovskite sensitizer. Recently, Xiao reported on an interdiffusion method to prepare pin-hole free perovskite films using a low temperature solution process, yielding 15.4% of the PSC efficiency.[25] However, the mesoporous $TiO_2$ photoanode with hundreds of nanometers of the thickness, is an important factor for the solution process to match with the preparation of perovskites, and the perovskite is usually hard to fill into the $TiO_2$ film.[21-24] On the other hand, Snaith reported an efficiency of 15.4% PSC by a vapour deposition,[4] which could obtain thin and homogeneous $CH_3NH_3PbI_3$ film on the surface of the $TiO_2$ with a planar structure. However, the thickness of the $TiO_2$ film should be thinner than the electron diffusion length of the $CH_3NH_3PbI_3$ to realize the separation of the electron and hole. The planar structure would lead to a waste of the intrinsic and high surface area of the $TiO_2$ nanoparticles. Furthermore, Etgar reported a HTM-free PSC with high power conversion efficiency of 8%,[26] due to that holes are extracted significantly more efficiently than electrons in $CH_3NH_3PbI_3$.[27] Recently, a 10.49% power conversion efficiency has

been reported for HTM-free PSCs confirming that the $TiO_2/CH_3NH_3PbI_3$/Au cell is an efficient heterojunction cell.[28]

Therefore, here we report on an in situ preparation of perovskite-sensitized $TiO_2$ nanofibers (TNFs) by using electrospun lead-doped TNFs, and preparation photoanodes for use in the PSCs by adding a film formation processes. Firstly, lead acetate is homo-dissolved into the mixture for electrospun, and then electrospinning Pb-doped TNFs. Secondly, the TNF&PbO is obtained after a film forming and sintering. Thirdly, the TNF&PbO is dipped in a HI acid solution, after the full reaction, drying, and the TNF&$PbI_2$ is achieved. Moreover, additional spin-coating $PbI_2$ on the TNF&$PbI_2$ can cover the shortage of the in situ method. Finally, the TNF&$PbI_2$ is soaked in a solution of $CH_3NH_3I$ and rinsed with isopropyl alcohol, after drying, the TNF&$CH_3NH_3PbI_3$ is gained by the in situ method. **Figure 1** shows the schematic diagram of the preparation processes for the PSC1 and PSC2. The PSC2 obtains an efficiency of 9.03% without any hole transporting materials.

## Experimental section

### Materials

Polyvinylpyrrolidone (PVP, Mw=1,300,000), isopropyl alcohol, acetic acid, titanium tetraisopropanolate (TTIP), lead acetate, acetone, methanol, ether, hydroiodic acid (45 wt.% in water), methylamine (30% in methanol), lead iodide ($PbI_2$), N,N-dimethylformamide (DMF), tetrabutyl titanate, and Triton X-100 were purchased from Shanghai Chemical Agent Ltd., China (Analysis purity grade). The above agents were used without further purification. The $CH_3NH_3I$ was prepared by reacting 20 mL hydroiodic acid (45 wt.% in water) and 20 mL methylamine (30% in methanol) in a 250 ml round-bottomed flask at 0 °C for 2 h with stirring. Then the

resulting solution was evaporated at 50 °C for 1 h. The precipitate was washed three times with diethyl ether, dried at 60 °C under a vacuum oven for 24 h, and used without further purification.

**Electrospun preparation of Pb-doped TNFs**

Lead acetate was dissolved into acetic acid to form a saturated lead acetate solution at room temperature (20 °C). PVP (100 mg) was dissolved into a mixture of isopropyl alcohol (0.6 mL) and aforementioned saturated lead acetate solution (0.4 mL). Under constant stirring, TTIP (0.2 mL) was added to the mixture for electrospun. The electrospun mixture was fed at a rate of approximately 1.0 $mL \cdot h^{-1}$ through a stainless-steel syringe pipette needle carrying a potential of +15.0 kV. Fibers were collected on a sheet of electrically grounded aluminum foil placed 15 cm below the syringe tip. The resultant fibrous mat was collected and then dried at room temperature under ambient atmosphere, yielding Pb-doped TNF mat. For comparison, the aforementioned saturated lead acetate solution was replaced by a pure acetic acid for the electrospun mixture, then obtaining pure TNF mat.

**In situ preparation of photoanodes**

The aforementioned pure TNF and Pb-doped TNF mats without sintering were cut into slices with a size dimension of 0.5 cm × 1.0 cm, then respectively placing on the cleaned FTO glass (1.5 cm × 2 cm, 8 $\Omega \cdot sq^{-1}$, NSG). After that , a drop of tetrabutyl titanate (3 mM) in isopropyl alcohol with a small quantity of Triton X-100 was dropped into the slice and then dried at room temperature, after sintered at 450 °C for 30 min, obtaining pure TNF and TNF&PbO films. The TNF&PbO film was further dipped in a HI solution (0.5 $mol \cdot L^{-1}$), after drying under ambient atmosphere, obtaining TNF&$PbI_2$ film. The $PbI_2$ solution in DMF (462 $mg \cdot mL^{-1}$) was spin-coated on the pure TNF and TNF&$PbI_2$ films, after drying at 80 °C for 6 h in the vacuum drying oven, the films were dipped in a solution of $CH_3NH_3I$ in isopropyl alcohol (10 $mg \cdot mL^{-1}$)

for 20 s and rinsed with isopropyl alcohol. After drying at 60 °C for 30 min in the vacuum drying oven, the TNF&$CH_3NH_3PbI_3$ photoanodes based on pure TNFs and Pb-doped TNFs were achieved.

**Solar cell fabrication**

Gold (100 nm) was sputtered on top of the TNF&$CH_3NH_3PbI_3$ photoanode to form the back contact by using a magnetron sputtering equipment (ETD-2000M, Beijing Elaborate Technology Development Ltd., China) to fabricate the PSC. It should be noted that the hole transporting material was absent in the PSC. The PSCs based on pure TNFs and Pb-doped TNFs, were described as PSC1 and PSC2, respectively.

**Characterizations and measurements**

The surface morphologies of samples were observed using a transmission electron microscope (TEM, JEOL-JSM-2100) operating at 200 kV and scanning electron microscopy (SEM, JEOL-JSM-6701F) operating at 10 kV. The phase identification of the products was conducted with powder X-ray diffraction (XRD, BRUKER D8-ADVANCE), by which the products were collected together from the FTO glass and following a grinding process. Ultraviolet to visible (UV-Vis) absorbance spectra of the samples were performed with an Agilent 8453 UV-Vis diode array spectrophotometer. Cyclic voltammetry (CV) was carried out on a computer-controlled Autolab potentiostat (Type III) in a solution of tetrabutylammonium hexafluorophosphate ($TBAPF_6$) (0.1 M) in anhydrous acetonitrile at a scan rate of 100 mV s at room temperature under argon protection. A FTO glass electrode was used as the working electrode (WE), each materials were deposited on the WE. A platinum wire was used as the counter electrode. As a reference electrode (RE), a silver wire coated with AgCl was used. After each measurement, the RE was calibrated with ferrocene.

The electrochemical impedance spectroscopy (EIS) of the PSC was performed using a CHI660D (Shanghai Chenhua Device Company, China) electrochemical measurement system at a constant temperature of 20 °C in ambient atmosphere under dark, and the impedance data covered a frequency range of 1-$10^5$ Hz with 5 mV of amplitude with 0.6, 0.7, 0.8, or 0.9 V bias potential, respectively. The incident monochromatic photon-to-current conversion efficiency (IPCE) curves were measured with a solar cell QE/IPCE measurement system (Solar Cell Scan 100, Beijing Zolix Instruments Co. Ltd., China). The photocurrent density-voltage (*J-V*) characteristic of the PSC was carried out using a computer-controlled CHI660D under illumination by a solar simulator (CEL-S500, Beijing Ceaulight Science and Technology Ltd., China) in ambient atmosphere. The incident light intensity was set under 100 $mW \cdot cm^{-2}$ (AM 1.5), and a black mask (0.40 $cm^2$) was used on top of the device to control the active cell area for the light irradiation.

## Results and discussion

**Figure 2** a shows the XRD pattern of the pure TNFs after sintered at 450 °C for 30 min, where the characteristic diffraction peak at 2θ of 25.3º for titania anatase (101) crystal face is observed, and all sharp peaks can be indexed as titania anatase (Joint Committee on Powder Diffraction Standards (JCPDS) card no. 21-1272). **Figure 2** b demonstrates the XRD pattern of the TNF&PbO, whereas the characteristic diffraction patterns at 28.5, 31.8, 36.1, 50.9, and 56.7 º are from the PbO, corresponding to the data in JCPDS card no. 78-1666. After dipping in the HI solution, the PbO was transformed into $PbI_2$ behind the chemistry of $PbO + 2HI \rightarrow PbI_2 + H_2O$ (**Figure 2** c). The $K_{sp}$ of the $PbI_2$ is about $1.39 \times 10^{-8}$ under 298 K of the temperature (Handbook of Chemisty and Physics, 1982-1983.63 th, Edition. B-242), which can benefit this

transformation. The crystalline phase of $PbI_2$ can be observed at 12.6, 25.7, 34.0, 39.5, and 52.3 º, which are identified to be the (001), (002), (102), (003), and (004) diffraction signals, respectively, according to the JCPDS card no. 73-1750. After soaking in the $CH_3NH_3I$ solution, the $PbI_2$ was changed to $CH_3NH_3PbI_3$ (**Figure 2** d). Strong diffraction peaks are observed at approximately 14.2, 20.0, 23.6, 24.6, 28.5, 31.9, 35.0, 40.6, and 43.2°, respectively corresponding to the reflections from (110), (112), (211), (202), (220), (310), (312), (224), and (314) crystal planes of the tetragonal perovskite structure.[29] And the characteristic diffraction peaks of the TNF are retained but weakened due to the TNF was covered with the $CH_3NH_3PbI_3$. The XRD patterns indicate that the perovskite sensitized TNF was successfully prepared through the in situ method, the in situ processes showed as below: $Pb(CH_3COO)_2 \rightarrow PbO \rightarrow PbI_2 \rightarrow CH_3NH_3PbI_3$.

**Figure 3** a and e show the TEM and SEM images of the pure TNF with a diameter of about 100 nm. **Figure 3** b displays that the PbO was doped in the TNF. A large number of holes evenly distribute on the surface of the TNF due to the PbO fell out of the TNF surface by the ultrasonic dispersion for the TEM measurement, similar phenomena appear in **Figure 3** c and d. After soaking in the $CH_3NH_3I$ solution, a mass of $CH_3NH_3PbI_3$ nanoparticles evenly decorate around the TNF (**Figure 3** d). **Figure 3** f shows the SEM image of the TNF&$CH_3NH_3PbI_3$ (without ultrasonic dispersion), it is obvious that the TNFs were decorated very well by the $CH_3NH_3PbI_3$ nanoparticles. These phenomena combining with the XRD results illustrate that the perovskite sensitized TNFs can be successfully prepared by the in situ method.

**Figure 4** a and b show the SEM images of the pure TNF and TNF&$CH_3NH_3PbI_3$ placed on the FTO glass substrates with the film formation processes. The diameter of the pure TNF is larger than that of in **Figure 3** e (without the film formation processes), this is due to the pure

TNF mat without sintering could be dissolved in the tetrabutyl titanate isopropyl alcohol solution, however, the solvent of isopropyl alcohol evaporated quickly resulting in a protection of the nanofibrous structure. Moreover, the tetrabutyl titanate could produce lots of $TiO_2$ nanoparticles after the sintering, leading to a good connection among the TNFs and FTO glass. The same phenomenon appears in **Figure 4** b, but the diameter has little change owing to the Pb doping. **Figure 4** c and d show the top-view and cross-sectional SEM images of the PSC2 through the $PbI_2$ in situ yielding and device preparing processes. The nanofibrous structure looms through the homogeneous Au nanoparticles on the $CH_3NH_3PbI_3$ film. The thickness of the TNF&$CH_3NH_3PbI_3$ film is about 5.0 μm. The $CH_3NH_3PbI_3$ has a diffusion length of 129 ± 41 nm for electrons,[8] which requests that the thickness of the $TiO_2$ films should be thinner than the electron diffusion length in a planar structure. However, in the device of PSC2, the electrospun TNFs can provide direct pathways for the rapid collection and transmission of photogenerated electrons,[20] and the TNF film is well filled and contacted with the $CH_3NH_3PbI_3$ according to the Pb-doped TNFs and in situ method, which is beneficial to the separation and transmission of the electron and hole, resulting in a very thick $TiO_2$ film could still work in the PSC. The thick $TiO_2$ film could take full advantage of the large surface area of the TNFs, leading to a high sunlight absorption and a high photovoltaic performance. However, there are some TNFs and $TiO_2$ nanoparticles reveal out of the surface of the perovskite sensitized photoanode if only prepared by the in situ method, which will directly contact with the Au electrode by the subsequent solar cell fabrication, resulting in an unwished increase of the electron recombination. For this consideration, additional spin-coating $PbI_2$ on the TNF&$PbI_2$ can cover the shortage of the in situ method. Moreover, introduction of the $CH_3NH_3PbI_3$ film well-covered on the surface of the TNF&$CH_3NH_3PbI_3$ film, would further influence the performance of the PSC.

**Figure 5** compares the UV-Vis absorption spectra of the pure TNF and TNF&$CH_3NH_3PbI_3$ films prepared on the FTO glass substrates. From the **Figure 5** a, the pure TNF film has a strong absorption at the 320 nm. The TNF&$CH_3NH_3PbI_3$ film has an additional broad absorption at around 400-800 nm.[2,29] The broad absorption window overlapping with the maximum irradiance of the solar spectrum ensures efficient photon harvesting, which may eventually lead to a high photocurrent. The optical band gap energy ($E_g$) of each materials was calculated by the equation of $E_g = 1240/\lambda$, in which the $\lambda$ value was measured by UV-Vis absorption spectra (**Figure 5** a). The $E_g$ values were listed in **Table 1**. The $E_g$ of the TNF film is demonstrated to be 3.25 eV. The $E_g$ of the $CH_3NH_3PbI_3$ deposited on the TNF film is determined to be 1.55 eV, which presents that the optical absorption in the perovskite sensitizer occurs via a direct transition.[30,31] The electrochemical properties of each materials were studied by the CV measurement, and the results were shown in **Figure 5** b, c, and d. The highest occupied molecular orbital (HOMO) and the lowest unoccupied molecular orbital (LUMO) levels were estimated from the oxidation potential ($E_{ox}$) according to the empirical formulas of HOMO = - ($E_{ox}$ + 4.80 - $E_{ox}$(Ferrocene)) and LUMO = HOMO + $E_g$, and the results were listed in **Table 1**. According to the results, the band positions are well aligned for the charge separation, the photon-generated electrons from the excited perovskite $CH_3NH_3PbI_3$ can be quickly transfered to the conductive band (CB) of semiconductor TNF, and forming the photo-current by the external circuit.

Electrochemical impedance spectroscopy (EIS) was used to characterize the internal resistance and charge transfer kinetics of the solar cell,[32] in which the potential bias was applied from 0.6 to 0.9 V in the dark in the frequency range from $10^5$ to 1 Hz, as shown in **Figure 6**. The equivalent circuit of this model (inset of **Figure 6**) has been already reported.[33-35] According to the simplified transmission line model, $R_S$ is the series resistance of the device, $R_1$ is the

charge-transfer resistance at the Au/$CH_3NH_3PbI_3$ interface, while $R_2$ (the main arc) is the charge-transfer resistance at the $CH_3NH_3PbI_3$/TNF interface. The constant phase elements ($C_1$ and $C_2$) are frequently used as substitutes for the capacitors in an equivalent circuit to fit the impedance behavior of the electrical double layer more accurately while the double layer does not behave as an ideal capacitor.[33-35] **Table 2** shows the impedance parameters obtained from the Z-view software analyses of the EIS data. The values of $R_S$, $R_1$, and $R_2$ decrease with the increasing the bias potential, due to the Fermi level in the $TiO_2$ or TNF is elevated at the forward bias which is beneficial to the easy electron flow across the $CH_3NH_3PbI_3/TiO_2$ or $CH_3NH_3PbI_3$/TNF interface. Under the same bias potential, The $R_S$, $R_1$, and $R_2$ values of the PSC2 are lower than those of the PSC1, especially for the $R_2$, owing to the TNF in the PSC2 could provide direct pathways for the rapid collection of photogenerated electrons and the high carrier mobility of the $CH_3NH_3PbI_3$ was well contacted and filled up in the TNF film, which could reduce the device resistance and enhance the separation and transmission rates of the electron and hole. The lower resistances could result in a more effective and rapid transporting ability for the electron and hole, which would further improve the performance of the PSC especially the fill factor. Additionally, the value of the $C_1$ or $C_2$ is closely related to the surface area, the higher the the $C_1$ or $C_2$ value, the larger the surface area.[36,37] The little difference of the $C_1$ value for the two devices due to the similar interface structure (Au/$CH_3NH_3PbI_3$ interface). However, the value of $C_2$ (0.94 $mF \cdot cm^{-2}$) for the PSC2 is higher than that of the PSC1 (0.83 $mF \cdot cm^{-2}$), this might be owing to its larger surface area of the TNF in the PSC2, which can promote the performance of the PSC device.

The incident monochromatic photon-to-current conversion efficiency (IPCE) of the PSC1 and PSC2 were characterized and are shown in **Figure 7** a, which reflects the light response of

the PSC and is directly related to the short-circuit current density ($J_{SC}$). The higher the IPCE, the higher the $J_{SC}$. The two PSCs show a wide light response from 350 nm to higher than 750 nm, with the maximum at ca. 550 nm. The IPCE of the PSC2 is higher than that of the PSC1, due to that more $CH_3NH_3PbI_3$ was filled into the TNF to absorb and utilize more sunlight, the well contact between the TNF and perovskite resulted in a quick and efficient separation and transmission of the electron and hole. These results were in agreement with the UV-Vis absorption spectra, EIS tests, and following *J-V* measurements. The photovoltaic properties of PSCs were measured under full sunlight illumination (100 $mW \cdot cm^{-2}$, AM1.5 G) and in dark, which were reproduced many times without obvious change. As can be seen in **Figure 7** b, the PSC1 produces a cell efficiency of 6.77%. The photovoltaic properties of the PSC2 are observably increased due to the $CH_3NH_3PbI_3$ well contacted and filled into the TNF film. As a result, the PSC2 demonstrates a higher $J_{SC}$ value of 19.36 $mA \cdot cm^{-2}$, open-circuit voltage ($V_{OC}$) of 0.88 V, fill factor (*FF*) of 0.53, and supplies a cell efficiency of 9.03%, even though the hole transporting material is absent in the PSC.

## Conclusions

In summary, Pb-doped TNFs were fabricated by the electrospun method, and then in situ preparation perovskite-sensitized photoanode for the PSC. Because of the electrospun TNFs can provide direct pathways for the rapid collection and transmission of photogenerated electrons, and the excellent contacting between the TNFs and perovskite can be beneficial to the separation and transmission of the electron and hole, the as-prepared photoanode could be much thicker than that of prepared by conventional solution processes or vapour deposition. These results could observably enhance the absorption of sunlight due to taking full advantage of the high

surface area of the TNFs and $TiO_2$ nanoparticles. High performance PSC with 9.03% of the cell efficiency was acquired without any HTMs. The performances of the in situ prepared PSC would further increase after optimizing the thickness of the photoanode, changing the organometallic three halide perovskite to the mixed halide perovskite, and adding HTMs into the device.

## Acknowledgments

The authors appreciate funding from National Natural Science Foundation of China (21274082 and 21073115) and Shanxi Province (2012021021-3), the Program for New Century Excellent Talents in University (NCET-10-0926), Scientific and Technologial Innovation Programs of Higher Education Institutions in Shanxi, and the Scientific Research Start-up Funds of Shanxi University (020351801003).

## Notes and references

*Institute of Molecular Science, Shanxi University, Taiyuan 030006, P. R. China.

E-mail: ymxiao@sxu.edu.cn (Yaoming Xiao); han_gaoyis@sxu.edu.cn (Gaoyi Han)

1 J. Burschka, N. Pellet, S. Moon, R. Humphry-Baker, P. Gao, M. Nazeeruddin and M. Grätzel, *Nature*, 2013, **499**, 316-319.

2 J. Heo, S. Im, J. Noh, T. Mandal, C. Lim, J. Chang, Y. Lee, H. Kim, A. Sarkar, M. Nazeeruddin, M. Grätzel and S. Seok, *Nature Photon.*, 2013, **7**, 486-491.

3 J. Ball, M. Lee, A. Hey and H. Snaith, *Energy Environ. Sci.*, 2013, **6**, 1739-1743.

4 M. Liu, M. Johnston and H. Snaith, *Nature*, 2013, **501**, 395-398.

5 M. Lee, J. Teuscher, T. Miyasaka, T. Murakami and H. Snaith, *Science*, 2012, **338**,

643-647.

6 M. He, D. Zheng, M. Wang, C. Lin and Z. Lin, *J. Mater. Chem. A*, 2014, **2**, 5994-6003.

7 H. Kim, I. Mora-Sero, V. Gonzalez-Pedro, F. Fabregat-Santiago, E. Juarez-Perez, N. Park and J. Bisquert, *Nature Commun.*, 2013, **4**, 2242 1-7.

8 S. Stranks, G. Eperon, G. Grancini, C. Menelaou, M. Alcocer, T. Leijtens, L. Herz, A. Petrozza and H. Snaith, *Science*, 2013, **342**, 341-344.

9 H. Choi, J. Jeong, H. Kim, S. Kim, B. Walker, G. Kim and J. Kim, *Nano Energy*, 2014, **7**, 80-85.

10 E. Edri, S. Kirmayer, D. Cahen and G. Hodes, *J. Chem. Phys. Lett.*, 2013, **4**, 897-902.

11 J. Qiu, Y. Qiu, K. Yan, M. Zhong, C. Mu, H. Yan and S. Yang, *Nanoscale*, 2013, **5**, 3245-3248.

12 P. Qin, S. Paek, M. Dar, N. Pellet, J. Ko, M. Grätzel and M. Nazeeruddin, *J. Am. Chem. Soc.*, 2014, **136** (24), 8516-8519.

13 Z. Tian, J. Voigt, J. Liu, B. Mckenzie and H. Xu, *J. Am. Chem. Soc.*, 2003, **125**, 12384-12385.

14 Y. Xiao, J. Wu, G. Yue, G. Xie, J. Lin and M. Huang, *Electrochim. Acta.*, 2010, **55**, 4573-4578.

15 B. Liu and E. Aydil, *J. Am. Chem. Soc.*, 2009, **131**, 3985-3990.

16 Z. Miao, D. Xu, J. Ouyang, G. Guo, X. Zhao and Y. Tang, *Nano Lett.,* 2002, **2**, 717-720.

17 B. Tan and Y. Wu, *J. Phys. Chem. B*, 2006, **110**, 15932-15938.

18 X. Feng, K. Shankar, M. Paulose and C. Grimes, *Angew. Chem.*, 2009, **121**, 8239-8242.

19 J. Wu, Y. Xiao, G. Yue, Q. Tang, J. Lin, M. Huang, Y. Huang, L. Fan, Z. Lan, S. Yin and T. Sato, *Adv. Mater.*, 2012, **24**, 1884-1888.

20 X. Sheng, D. He, J. Yang, K. Zhu and X. Feng, *Nano Lett.*, 2014, **14**, 1848-1852.

21 D. Liu and T. Kelly, *Nature Photon.*, 2014, **8**, 133-138.

22 A. Dualeh, N. Tétreault, T. Moehl, P. Gao, M, Nazeeruddin and M. Grätzel, *Adv. Funct. Mater.*, 2014, **24**, 3250-3258.

23 G. Eperon, V. Burlakov, P. Docampo, A. Goriely and H. Snaith, *Adv. Funct. Mater.*, 2014, 24, 151-157.

24 K. Wojciechowski, M. Saliba, T. Leijtens, A. Abate and H. Snaith, *Energy Environ. Sci.*, 2014, **7**, 1142-1147.

25 Z. Xiao, C. Bi, Y. Shao, Q. Dong, Q. Wang, Y. Yuan, C. Wang, Y. Gao and J. Huang, *Energy Environ. Sci.* 2014, DOI: 10.1039/c4ee01138d.

26 W. Laban and L. Etgar, *Energy Environ. Sci.*, 2013, **6**, 3249-3253.

27 E. Edri, S. Kirmayer, A. Henning, S. Mukhopadhyay, K. Gartsman, Y. Rosenwaks, G. Hodes and D. Cahen, *Nano Lett.*, 2014, **14**, 1000-1004.

28 J. Shi, J. Dong, S. Lv, Y. Xu, L. Zhu, J. Xiao, X. Xu, H. Wu, D. Li, Y. Luo and Q. Meng, Appl. Phys. Lett., 2014, **104**, 063901.

29 Y. Zhao and K. Zhu, *J. Phys. Chem. Lett.*, 2013, **4**, 2880-2884.

30 H. Lin, C. Huang, W. Li, C. Ni, S. Shah and Y. Tseng, *Appl. Catal. B-Environ.*, 2006, **68**, 1.

31 H. Kim, C. Lee, J. Im, K. Lee, T. Moehl, A. Marchioro, S. Moon, R. Humphry-Baker, J. Yum, J. Moser, M. Grätzel and N. Park, *Sci. Rep.*, 2012, **2**, 591.

32 Y. Zhao, J. Zhai, J. He, X. Chen, L. Chen, L. Zhang, Y. Tian, L. Jiang and D. Zhu, *Chem. Mater.*, 2008, **20**, 6022-6028.

33 H. Kim, J. Lee, N. Yantara, P. Boix, S. Kulkarni, S. Mhaisalkar, M. Grätzel and N. Park, *Nano Lett.*, 2013, **13**, 2412-2417.

34 G. Niu, W. Li, F. Meng, L. Wang, H. Dong and Y. Qiu, *J. Mater. Chem. A*, 2014, **2**, 705-710.

35 Y. Xiao, G. Han, Y. Chang, H. Zhou, M. Li and Y. Li, *J. Power Sources*, 2014, **267**, 1-8.

36 Y. Xiao, J. Wu, J. Lin, S. Tai and G. Yue, *J. Mater. Chem. A*, 2013, **1**, 1289-1295.

37 Y. Xiao, G. Han, Y. Li, M. Li and Y. Chang, *J. Mater. Chem. A*, 2014, **2**, 3452-3460.

**Figure and Table Captions**

**Table 1** Optical and electrochemical properties of the TNF and $CH_3NH_3PbI_3$.

**Table 2** EIS results of the PSC1 and PSC2.

**Figure 1 S**chematic diagram of the preparation processes for the PSC1 and PSC2: nanofibers electrospinning (1); films forming (2); $PbI_2$ in situ yielding (3); devices preparing (4).

**Figure 2** XRD patterns of the pure TNF and products in the in situ preparation processes.

**Figure 3** TEM images of the pure TNF (a), TNF&PbO (b), TNF&$PbI_2$ (c), and TNF&$CH_3NH_3PbI_3$ (d), insets are the larger versions of (b) and (d) with a scale of 20 nm; SEM images of the pure TNF (e) and TNF&$CH_3NH_3PbI_3$ (f) without the film formation processes.

**Figure 4** SEM images of the photoanodes based on the pure TNF (a) and Pd-doped TNF (b), top-view (c) and cross-sectional (d) SEM images of the PSC2.

**Figure 5** UV-Vis adsorption spectra (a) of the pure TNF and TNF&$CH_3NH_3PbI_3$; CVs of Ferrocene (b), TNF (c), and $CH_3NH_3PbI_3$ (d), respectively.

**Figure 6** Nyquist plots of the PSC1 (a) and PSC2 (b); Inset is the equivalent circuit of the PSC.

**Figure 7** IPCE (a) and Photocurrent density-voltage characteristics (b) of the PSC1 and PSC2.

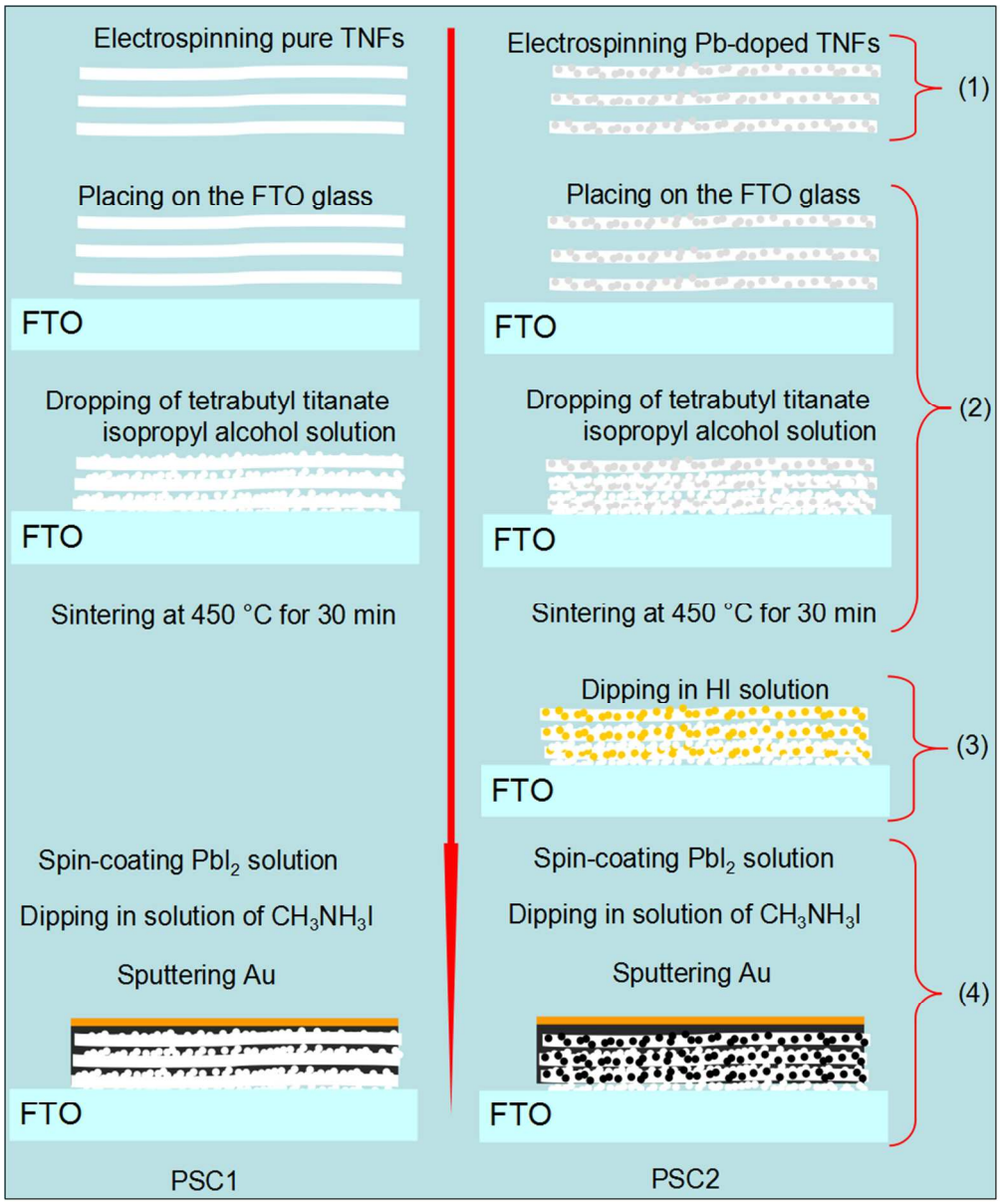


Figure 1 Schematic diagram of the preparation processes for the PSC1 and PSC2: nanofibers electrospinning (1); films forming (2); PbI2 in situ yielding (3); devices preparing (4).
267x320mm (96 x 96 DPI)

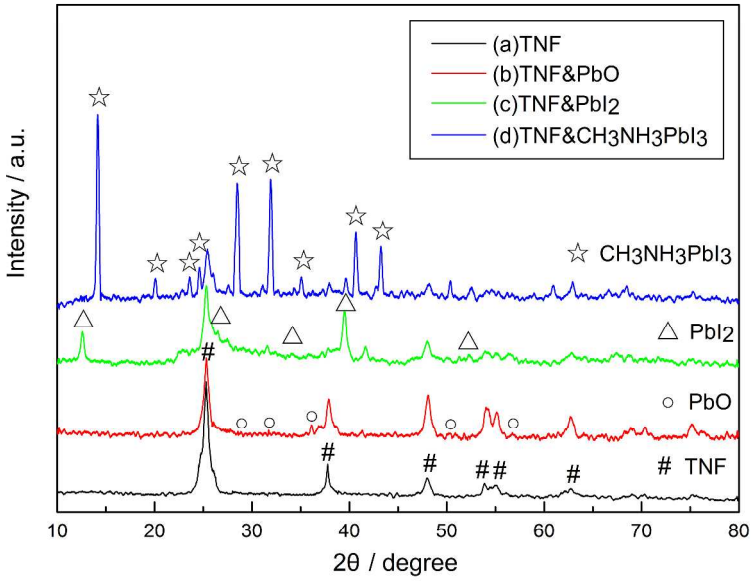


Figure 2 XRD patterns of the pure TNF and products in the in situ preparation processes.
1187x839mm (150 x 150 DPI)

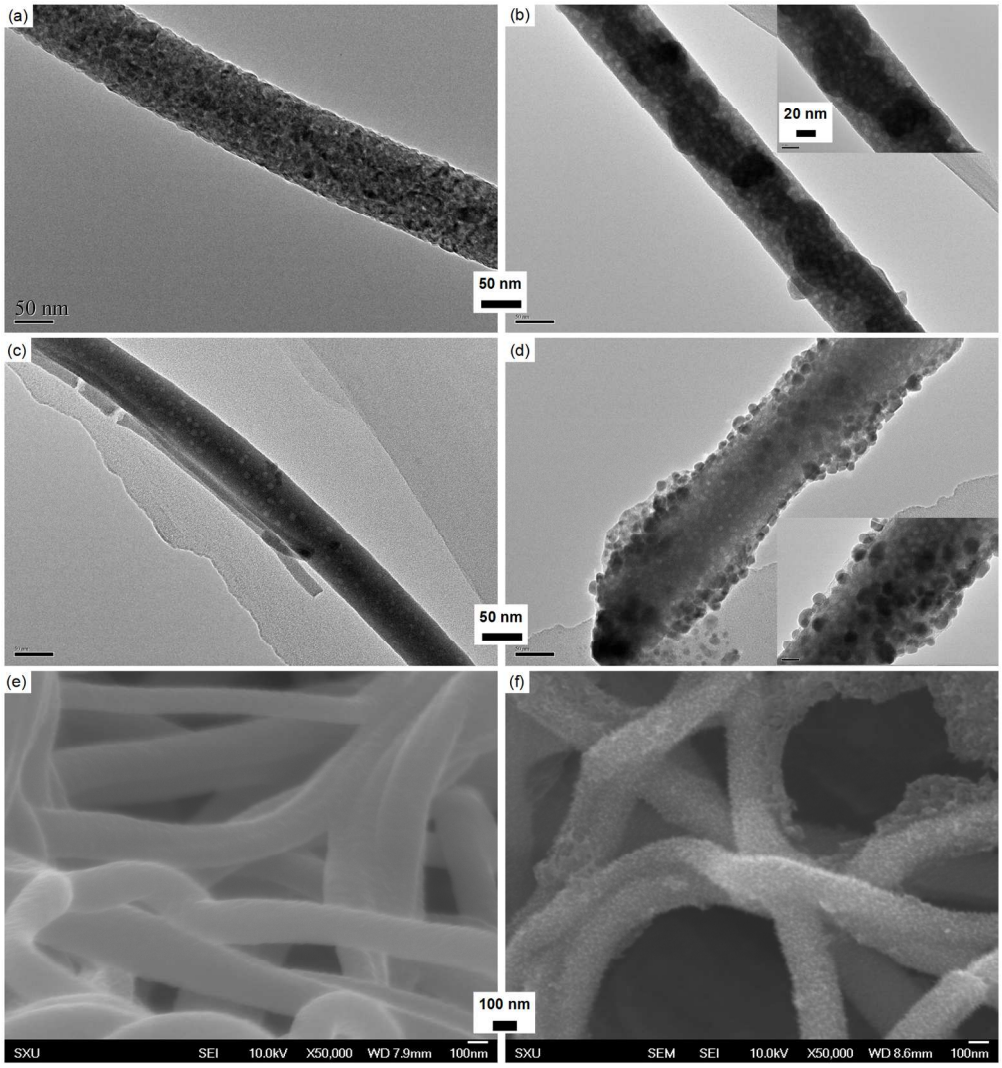


Figure 3 TEM images of the pure TNF (a), TNF&PbO (b), TNF&PbI2 (c), and TNF&CH3NH3PbI3 (d), insets are the larger versions of (b) and (d) with a scale of 20 nm; SEM images of the pure TNF (e) and TNF&CH3NH3PbI3 (f) without the film formation processes.
515x549mm (96 x 96 DPI)

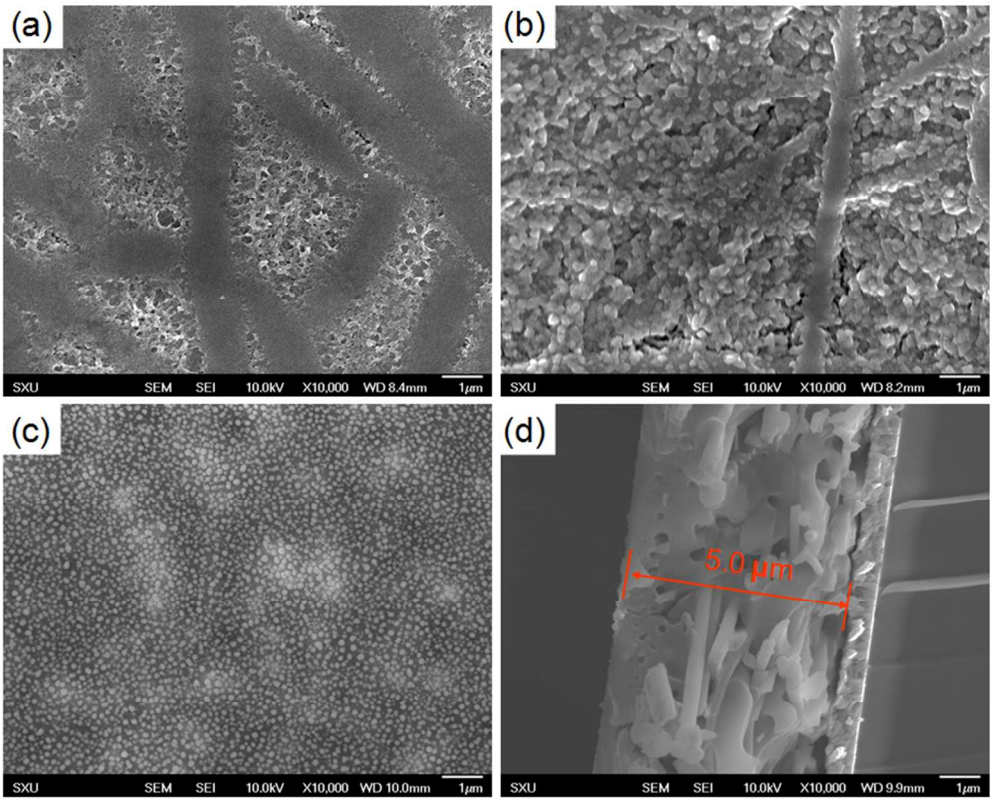


Figure 4 SEM images of the photoanodes based on the pure TNF (a) and Pd-doped TNF (b), top-view (c) and cross-sectional (d) SEM images of the PSC2.
245x197mm (96 x 96 DPI)

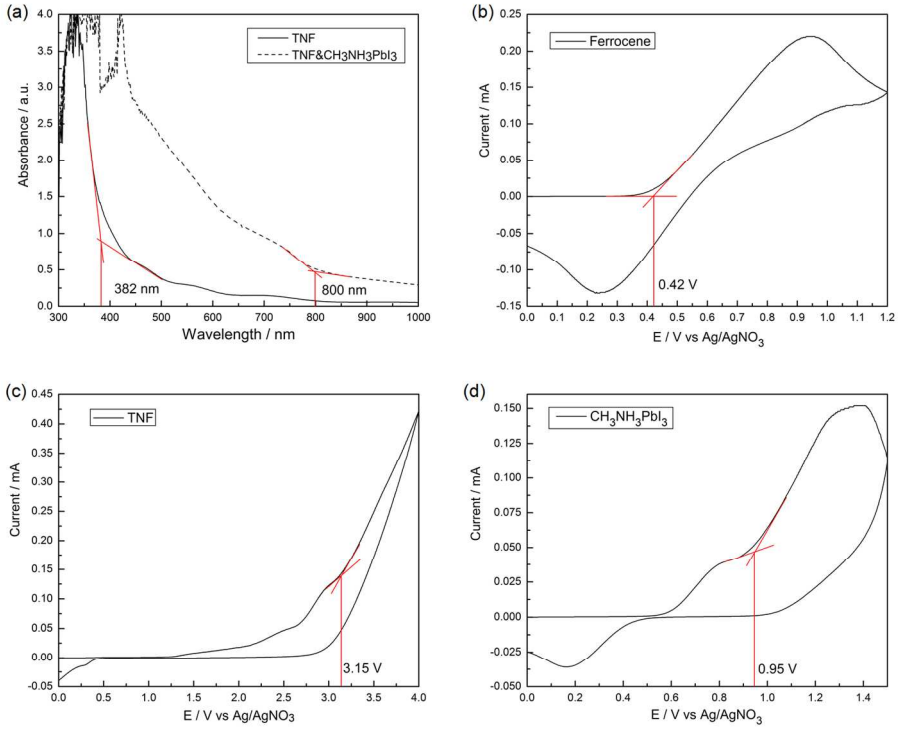


Figure 5 UV-Vis adsorption spectra (a) of the pure TNF and TNF&CH3NH3PbI3; CVs of Ferrocene (b), TNF (c), and CH3NH3PbI3 (d), respectively.
467x371mm (96 x 96 DPI)

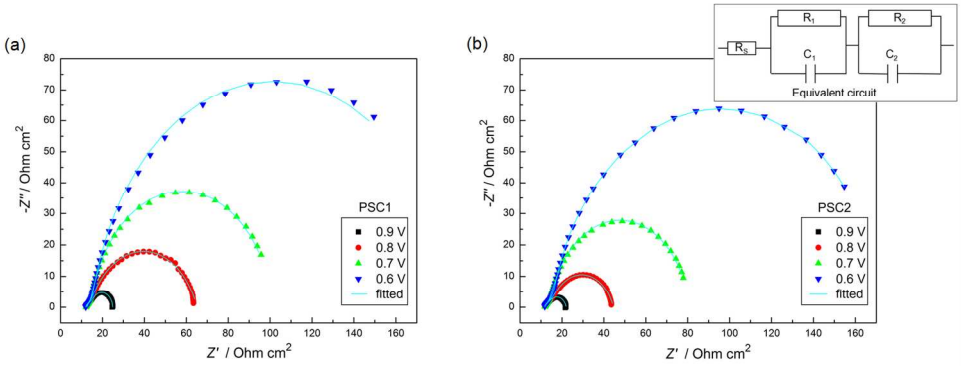


Figure 6 Nyquist plots of the PSC1 (a) and PSC2 (b); Inset is the equivalent circuit of the PSC.
485x189mm (96 x 96 DPI)

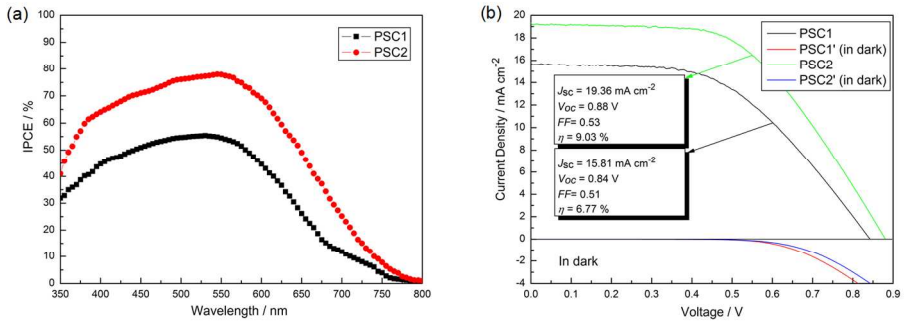


Figure 7 IPCE (a) and Photocurrent density-voltage characteristics (b) of the PSC1 and PSC2.
479x179mm (96 x 96 DPI)

**Table 1** Optical and electrochemical properties of the TNF and $CH_3NH_3PbI_3$.

| Sample | $\lambda^a$ (nm) | $E_g^b$ (eV) | $E_{ox}^c$ (V) | $E_{ox}$(Ferrocene) (V) | HOMO[d] (eV) | LUMO[e] (eV) |
|---|---|---|---|---|---|---|
| TNF | 382 | 3.25 | 3.15 | 0.42 | -7.53 | -4.28 |
| $CH_3NH_3PbI_3$ | 800 | 1.55 | 0.95 | 0.42 | -5.33 | -3.78 |

[a] λ measured by UV-Vis absorption spectra (**Figure 5** a); [b] $E_g = 1240/\lambda$;

[c] Oxidation potentials measured by cyclic voltammetry (**Figure 5** b, c, and d);

[d] HOMO = - ($E_{ox}$ + 4.80 - $E_{ox}$(Ferrocene)) eV; [e] LUMO = HOMO + $E_g$

**Table 2** EIS results of the PSC1 and PSC2.

| | bias potential (V) | $R_S$ ($\Omega \cdot cm^2$) | $R_1$ ($\Omega \cdot cm^2$) | $R_2$ ($\Omega \cdot cm^2$) | $C_1$ ($mF \cdot cm^{-2}$) | $C_2$ ($mF \cdot cm^{-2}$) |
|---|---|---|---|---|---|---|
| PSC1 | 0.9 | 12.18 | 1.15 | 4.86 | 0.71 | 0.83 |
| | 0.8 | 12.23 | 1.21 | 25.27 | 0.69 | 0.81 |
| | 0.7 | 12.26 | 1.34 | 43.46 | 0.70 | 0.80 |
| | 0.6 | 12.31 | 1.45 | 86.50 | 0.68 | 0.77 |
| PSC2 | 0.9 | 11.77 | 1.08 | 1.73 | 0.74 | 0.94 |
| | 0.8 | 11.81 | 1.19 | 14.77 | 0.75 | 0.92 |
| | 0.7 | 11.83 | 1.27 | 33.36 | 0.74 | 0.90 |
| | 0.6 | 11.85 | 1.36 | 78.61 | 0.72 | 0.89 |